JOURNAL OF MATERIALS SCIENCE 33 (1998) 1723–1736

# Non-metallic inclusions and their relation to the $J$-integral, $J_{\mathrm{i,\,phys}}$, at physical crack initiation for different steels and weld metals

P. DEIMEL, E. SATTLER
*Staatliche Materialprüfungsanstalt (MPA), Universität Stuttgart, 70569 Stuttgart, Germany*

For two types of steel, the heat-resistant 12% Cr–steel X 20 CrMoV 12 1 and the fine-grained pressure vessel steel 20 MnMoNi 5 5 (A 508 cl.3), a wide range of toughness values in the upper shelf was realized by different sulfur contents and the inclusion of similar weld metals. Additionally, the pressure vessel steel 22 NiMoCr 3 7 (A 508 cl.2) was also investigated. Tensile, fracture mechanics and Charpy V-notch impact tests, as well as detailed microstructural investigations with respect to the size distribution and density of non-metallic inclusions and precipitates, were carried out. In order to ensure ductile behaviour, a test temperature of 150 °C was chosen. The relevance of two quantitative relations available for the calculation of the $J$-integral, $J_{\mathrm{i,phys}}$, at physical crack initiation using tensile test data and microstructural parameters, were examined by comparison with the corresponding experimental $J_{\mathrm{i,phys}}$-values. Only one quantitative relation was able to give good agreement between calculated and experimental $J_{\mathrm{i,phys}}$-values. This holds not only for the base materials but also for the weld metals. The importance of the size and density of the non-metallic inclusions became quantitatively obvious with the consequence that their size times density is a decisive parameter for toughness. Observations of void initiation, growth and coalescence illustrate the fracture process. © *1998 Chapman & Hall*

## 1. Introduction and aim

Important properties of materials for the design of technical structures, with respect to safety against failure, are strength and toughness. These properties are mainly caused by the microstructure of the material and are usually characterized by values determined by means of technological tests. Taking into account that most structural parts include weld joints, the properties of the base material as well as of the weld joint have to be considered. In fracture mechanics, a characteristic frequently used for ductile materials is the $J$-integral and, in particular, $J_{\mathrm{i,phys}}$, the value of this integral at physical crack initiation.

Extensive investigations have been performed to improve the understanding of the microstructural deformation processes of ductile materials [1, 2]. Experiments on tensile specimens of different kinds of steels, titanium, aluminium and copper alloys [1] loaded to fracture or to different amounts of plastic deformation, revealed that the initiation of fracture and the fracture process show three successive stages during the course of which the particles present in the matrix, such as inclusions and precipitates, were generally found to be the microstructural constituents essential for the fracture process.

At first, voids begin to form by separation of particles from the matrix at their interface, or by cracking of particles when a critical strain is exceeded. Then these voids grow in the direction of maximum tensile stress and new voids nucleate while the load increases, and finally void coalescence occurs by necking or shearing of the material remaining between the voids. This is shown schematically in Fig. 1.

Based on these observations, quantitative formulations for each of the three stages of the fracture process were established, such as laws for void growth, as well as conditions for void nucleation and coalescence [3]. To obtain a general and quantitative description of the whole fracture process and to calculate toughness parameters for the case of ductile fracture behaviour, it is necessary to have a quantitative relation containing implicitly or explicitly the different formulations relevant for the individual phases of the fracture process.

Two relations directly or indirectly connecting microstructural parameters as well as parameters of the tensile test with fracture mechanics characteristics for crack initiation, have already been derived in mathematically closed form by Stroppe [4] and Hahn and Rosenfield [5]. In addition to these relations, the application of numerical methods increases simulating of fracture initation and the fracture process by using constitutive material models which approximate the geometrical and physical situation [6]. Furthermore, Lautridou and Pineau [7] investigated if a correlation exists between the critical value, $J_{\mathrm{Ic}}$, of the

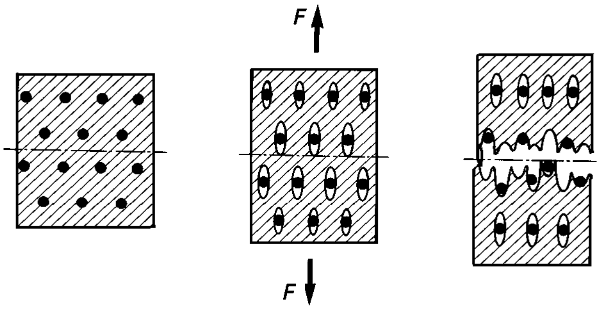

*Figure 1* Schematic representation of the formation of a ductile fracture surface (according to [4]).

$J$-integral or the associated crack opening and the distance of nearest neighbours for the case of non-metallic inclusions.

The aim of the present investigation was to apply both relations [4, 5] to base materials as well as weld metals. In order to be able to prove, by comparison with the experimental values, whether one or both of these relations are suitable for the quantitative prediction of the $J$-integral, $J_{\mathrm{i,phys}}$, a wide variety of toughness values represented by the absorbed energy in the upper shelf has to be realized. With two kinds of steel, differing in metallographic structure and field of application, together with the corresponding similar weld metals, this variation in toughness will be achieved. One steel is the heat-resistant 12% Cr–steel X 20 CrMoV 12 1, the other one the fine-grained pressure vessel steel 20 MnMoNi 5 5 corresponding to A 508 cl.3. For each type of steel, the sulfur content will be varied and, as a consequence, the importance of the non-metallic inclusions on $J_{\mathrm{i,phys}}$ quantitatively studied. Additionally, with respect to the base material, another pressure vessel steel 22 NiMoCr 3 7 corresponding to A 508 cl.2 was also investigated. Furthermore, the analysis of the fracture process itself will answer questions concerning the relevance of the assumptions upon which the two quantitative relations mentioned are based. The investigations were performed during a long-term project over a period of almost one decade. Previous papers [8, 9] have reported initial and spotlike results, with respect to the actual investigation and the overall aim, but these will be included here for comparison and for broadening the basis for proof.

## 2. Quantitative relations between the *J*-integral at physical crack initiation and microstructural as well as tensile test data

The two relations used for the calculation of the $J$-integral, $J_{\mathrm{i,phys}}$, at physical crack initiation (the relation of Stroppe [4] and that of Hahn and Rosenfield [5]) are based on the assumption that the process taking place at the crack tip at loading and the relations derived therefrom are transferable to the conditions for void nucleation at particles.

The Stroppe's relation was originally deduced for the calculation of $J_{\mathrm{Ic}}$ whereas that of Hahn and Rosenfield was originally formulated for the calculation of the fracture toughness, $K_{\mathrm{Ic}}$, and had to be transformed into a relation for $J_{\mathrm{i,phys}}$. Stroppe's relation, containing the average spatial spacing of the particles, a microstructural parameter whose determination is very sophisticated, had also to be transformed. A detailed description of the deduction and the modification of both relations was given elsewhere [8].

The Stroppe's relation, modified by Deimel *et al.* [8], is written as follows

$$J_{\mathrm{i,\,phys}} = \frac{k\varphi_{\mathrm{B}}^{n+1}}{\pi(n+1)\mathrm{e}^{\varphi_{\mathrm{B}}}}\frac{1}{N_{\mathrm{E}}D_0} \qquad (1)$$

The first term of the right-hand side of Equation 1 contains only quantities determined in a uniaxial tensile test ($\varphi_{\mathrm{B}}$ = true strain at fracture, $k$ = strength coefficient, $n$ = strain-hardening exponent); the second term contains microstructural parameters ($N_{\mathrm{E}}$ = average number of particles per unit area, $D_0$ = average diameter of the particles) determined on a polished metallographic section, a replica or a thinned foil.

Hahn and Rosenfield's relation, also modified by Deimel *et al.* [8], can be written as

$$J_{\mathrm{i,\,phys}} = \frac{2}{3}\,25.4\,\mathrm{mm}\,(1-\nu^2)R_{\mathrm{e}}\,\varphi_{\mathrm{B}}\,n^2 \qquad (2)$$

and contains only quantities which can be determined in the uniaxial tensile test ($\nu$ = Poisson's ratio, $R_{\mathrm{e}}$ = yield stress).

## 3. Experimental procedure and results

### 3.1. Materials

The experimental investigations were performed, as explained in Section 1, for two different categories of steel, the heat-resistant steel X 20 CrMoV 12 1, having a structure of tempered martensite, and the fine-grained structural steels 20 MnMoNi 5 5 and 22 NiMoCr 3 7, both with bainitic structure.

For the steel X 20 CrMoV 12 1, two components were available, namely a section of a seamless pressed tube having an inner diameter of 320 mm, a wall thickness of 36 mm and an overall length of 950 mm, as well as a seamless pressed thick-walled cylindrical vessel section with an inner diameter of 600 mm and a wall thickness of 95 mm containing a longitudinal and a circumferential similar weld seam. The realized welding parameters of the circumferential weld seam are compiled in Table I. The optimized material of the tube had a significantly lower sulfur content than the conventional material of the vessel section. In order to realize lower toughness conditions for the investigations, parts of the circumferential weld seam were aged at 550 °C for $10^4$ h. Chemical composition and heat treatment of the base materials and of the weld metal are shown in Tables II and III. For the vessel section, the position of the specimens for the determination of the mechanical and the fracture mechanics properties is shown schematically in Fig. 2. Specimens were taken from the seamless pressed tube in the same way.

The investigations on the steel 20 MnMoNi 5 5 were performed on a section of a forged slab having a low sulfur content of 0.003% S and a length of 700 mm, a width of 440 mm and a thickness of 370 mm. Two further slabs with similar geometrical dimensions and a similar amount of deformation by forging, but different sulfur contents (0.011% and 0.020% S) were fabricated to study the influence of sulphur content also for the fine-grained pressure vessel steel. Additionally, the base material 22 NiMoCr 3 7 was included which was available as a plate with a length of 3210 mm, a width of 623 mm and a thickness of 95 mm. As weld metal, a shape-welded cylindrical ring of the material 10 MnMoNi 5 5 was available with an inner diameter of 1235 mm, a wall thickness of 288 mm and an overall length of 5480 mm. The welding data are listed in Table IV. Chemical composition and heat treatment of the pressure vessel steels, as well as of the weld metal, are shown in Tables V and VI. For the slab with the low sulfur content, the position of the specimens for the determination of the mechanical and the fracture mechanics properties is illustrated schematically in Fig. 3 and was realized for the other base materials listed in Table V in the same way. The specimens for the mechanical and the fracture mechanics tests taken from the shape-welded material were situated transverse to the circumferential welding direction, as already shown for the X 20 CrMoV 12 1 similar weld metal, Fig. 2.

TABLE I Welding parameters of the X 20 CrMoV 12 1-similar weld seam

| | | |
|---|---|---|
| Root pass | In order to produce a multilayer single-U-groove weld, part of an already existing vessel was suitably grooved from the outside in circumferential direction leaving a thin bridge of the base material. Therefore, no welded root exists. | |
| Filler passes and final pass | Welding method | Single-pass, submerged-arc weld |
| | Welding filler material | MTS 4 DEW 3 mm diameter |
| | Voltage/current | 27 V/430–450 A |
| | Welding speed | 50 cm min$^{-1}$ |
| | Energy input per unit length | 14 600 J cm$^{-1}$ |
| | Submerged-arc weld flux | LW 320 Linde |
| | Preheat to temperature | 230–250 °C |
| | Cooling after welding to | 125–130 °C |

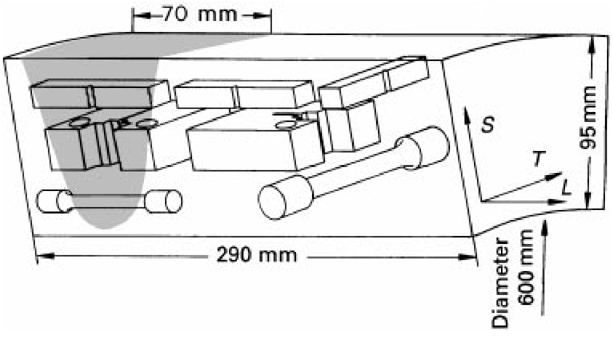

*Figure 2* Position of the specimens for the determination of mechanical characteristics as well as of fracture mechanics data for the X 20 CrMoV 12 1 base materials and the aged similar weld metal of the circumferential seam.

TABLE II Chemical composition (wt %) of the X 20 CrMoV 12 1 base materials and of the X 20 CrMoV 12 1-similar weld metal

| Material | C | Si | Mn | P | S | Cr | Mo | Ni | V | Al |
|---|---|---|---|---|---|---|---|---|---|---|
| X 20 CrMoV 12 1 (0.005% S) | 0.17 | 0.24 | 0.55 | 0.016 | 0.005 | 11.00 | 0.82 | 0.68 | 0.25 | – |
| X 20 CrMoV 12 1 (0.016% S) | 0.18 | 0.16 | 0.73 | 0.016 | 0.016 | 12.10 | 0.89 | 0.74 | 0.32 | – |
| X 20 CrMoV 12 1 | 0.16 | 0.38 | 1.96 | 0.020 | 0.005 | 10.60 | 0.93 | 0.77 | 0.21 | 0.01 |
| similar weld metal | Cu | W | Co | Nb | Sn | Ti | As | N | O | – |
| (550 °C/10$^4$ h) | 0.07 | 0.39 | 0.03 | $\ll$0.01 | < 0.01 | < 0.01 | 0.01 | 0.031 | 0.057 | – |

TABLE III Heat treatment of the X 20 CrMoV 12 1 base materials and of the X 20 CrMoV 12 1-similar weld metal

| Material | Heat treatment | | |
|---|---|---|---|
| X 20 CrMoV 12 1 (0.005% S) | Heat treatment of the seamless tube | Hardening<br>Tempering | 1050 °C/0.75 h/air<br>760–770 °C/2 h/air |
| X 20 CrMoV 12 1 (0.016% S) | Heat treatment of the seamless tube | Hardening<br>Tempering | 1050 °C/6 h/air<br>760–770 °C/6 h/air |
| | 1st tempering after welding of the longitudinal seam | | 740 °C/10 h/furnace |
| | 2nd tempering after welding of the circumferential seam | | 760 °C/10 h/furnace |
| X 20 CrMoV 12 1 similar weld metal (550 °C/10$^4$ h) | Heat treatment after welding | Cooling after welding to<br>Tempering<br>Holding time/cooling | 125–135 °C<br>760 °C<br>10 h/furnace |
| | Ageing | In the furnance | 550 °C/10$^4$ h |

## 3.2. Impact testing and tensile tests

Comparing the $C_v$–$T$ curves for the material X 20 CrMoV 12 1 in Fig. 4, it can be seen that at a temperature of 150 °C the base materials already are in the upper shelf of the absorbed energy and that the similar weld metal has achieved the upper shelf. The 20 MnMoNi 5 5 and 22 NiMoCr 3 7 base materials, as well as the shape-welded material 10 MnMoNi 5 5, are also in the upper shelf at 150 °C, Fig. 5. Therefore, ductile behaviour, a necessary assumption for the applicability of Equations 1 and 2, is realized at 150 °C for all the materials used. The tensile tests as well as the fracture mechanics tests were then realized at this temperature. For the two material groups, the characteristic data of the tensile test at room temperature and 150 °C, together with the absorbed energy, are compiled in Table VII.

## 3.3. Fracture mechanics

The fracture mechanics tests were performed using the single-specimen technique with partial unloading described in ASTM E 813-87. At each partial unloading, two quantities were determined, namely the $J$-integral and, from the crack length, the crack extension, $\Delta a$. The actual value of the $J$-integral was calculated either according to Section 9.1.2 of ASTM E 813-81, or according to a modified relation of Ernst *et al.* [10]. These two values are distinguished by the terms "ASTM" and "Ernst mod". In determining the corresponding value of crack growth, it must be noticed that shifting of the load line occurs with increasing crack

TABLE IV Welding parameters of the 10 MnMoNi 5 5 shape-welded material

| | |
|---|---|
| Welding method | Submerged arc welding with 4 tandem welding heads |
| Welding filler metal | 10 MnMoNi 5 5/4 mm diameter |
| Voltage/current | 30 V/600 A |
| Welding speed | 70 cm min$^{-1}$ |
| Energy input per unit length | 2–15.4 kJ cm$^{-1}$ |
| Fluoridbasic agglomerated weld flux | UV 14210 |
| Distance of the tandem welds | Approximately 25 mm |
| Welding direction | Screw line with a half-bead overlap |
| Interpass temperature | Approximately 150 °C |
| Temperature of the complete cylinder during the course of the welding process | 300 °C |

TABLE VI Heat treatment of the 20 MnMoNi 5 5 base materials as well as of the base material 22 NiMoCr 3 7 and the shape-welded material 10 MnMoNi 5 5

| Material | Heat treatment | |
|---|---|---|
| 20 MnMoNi 5 5 (0.003% S) | Hardening<br>Tempering | 920–935 °C/9 h/water<br>640–650 °C/10 h/air |
| 20 MnMoNi 5 5 (0.011% S/0.020% S) | Hardening<br>Tempering | 910–920 °C/4.75 h/water<br>640–645 °C/9 h/air |
| 22 NiMoCr 3 7 (0.006% S) | Hardening<br>Tempering | 900 °C/8 h/water<br>660 °C/9 h/air |
| 10 MnMoNi 5 5 shape-welded (520 °C/20 h) | Stress-relieving anneal | 520 °C/20 h |

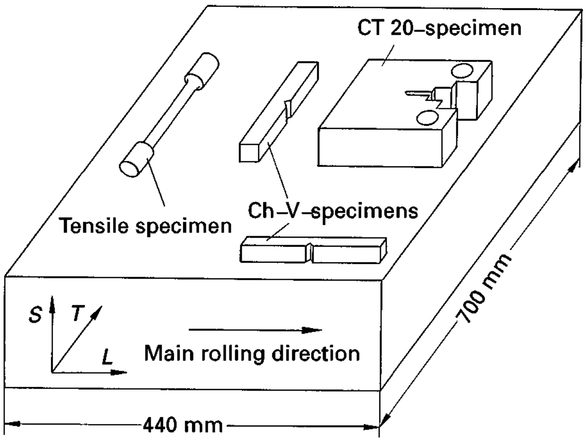

*Figure 3* Position of the specimens for the determination of mechanical characteristics, and the fracture mechanics data for the 20 MnMoNi 5 5 base materials, as well as for the base material 22 NiMoCr 3 7 and the shape-welded material 10 MnMoNi 5 5.

TABLE V Chemical composition (wt %) of the 20 MnMoNi 5 5 base materials as well as of the base material 22 NiMoCr 3 7 and the shape-welded material 10 MnMoNi 5 5

| Material | C | Si | Mn | P | S | Cr | Mo | Ni | Al (tot.) | Cu | V | Sn | N (tot.) | Ti |
|---|---|---|---|---|---|---|---|---|---|---|---|---|---|---|
| 20 MnMoNi 5 5 (0.003% S) | 0.19 | 0.25 | 1.40 | 0.007 | 0.003 | 0.09 | 0.49 | 0.80 | 0.023 | 0.07 | 0.010 | 0.004 | 0.010 | – |
| 20 MnMoNi 5 5 (0.011% S) | 0.19 | 0.26 | 1.33 | 0.007 | 0.011 | 0.05 | 0.51 | 0.79 | 0.010 | 0.05 | 0.009 | $<0.01$ | – | $<0.01$ |
| 20 MnMoNi 5 5 (0.020% S) | 0.20 | 0.09 | 1.04 | 0.010 | 0.020 | 0.09 | 0.49 | 0.78 | 0.009 | 0.06 | 0.010 | $<0.01$ | – | 0.012 |
| 22 NiMoCr 3 7 (0.006% S) | 0.18 | 0.23 | 0.71 | 0.006 | 0.006 | 0.45 | 0.68 | 0.77 | 0.02 | 0.18 | $<0.01$ | 0.01 | – | $<0.01$ |
| 10 MnMoNi 5 5 shape-welded (520 °C/20 h) | 0.10<br>W<br>$<0.01$ | 0.13<br>Co<br>0.03 | 1.27<br>Nb<br>$<0.01$ | 0.006<br>As<br>$\ll 0.01$ | 0.004<br>O<br>0.018 | 0.049 | 0.59 | 1.02 | 0.005 | 0.048 | 0.0012 | $<0.002$ | 0.013 | 0.0035 |

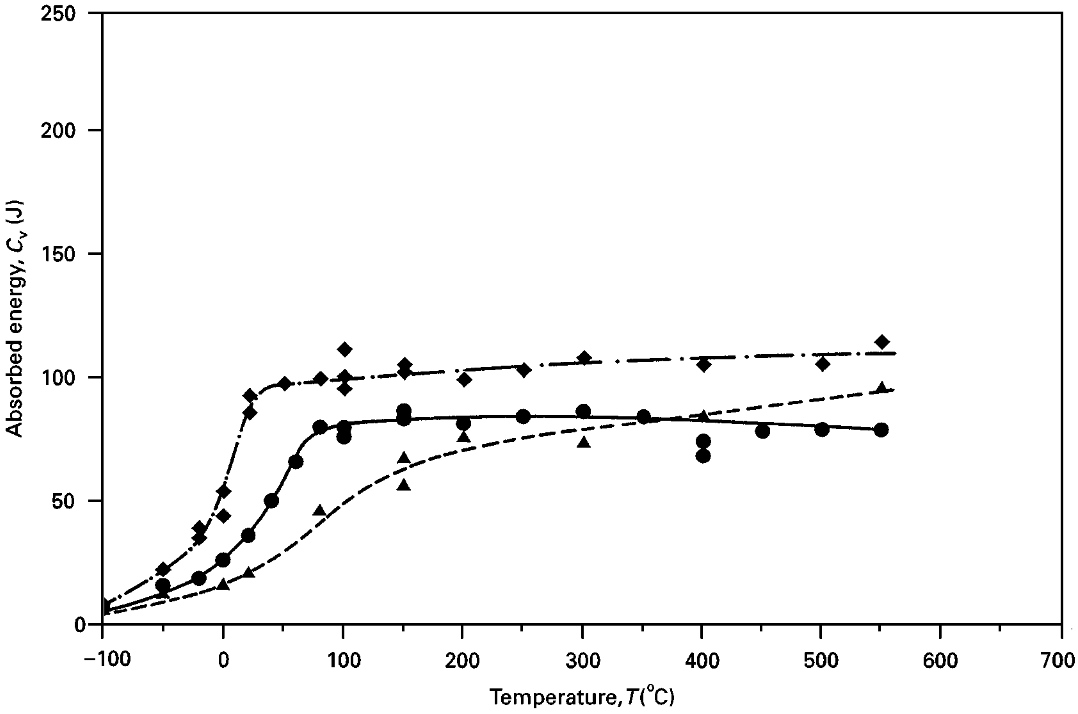

*Figure 4* $C_v$–$T$ curves for the X 20 CrMoV 12 1 base materials (◆, ●) as well as for the aged similar weld metal of the circumferential seam ▲. (◆) 0.005% S, transverse; (●) 0.016% S, transverse; (▲) 0.005% S, aged 550 °C/$10^4$ h, S-position.

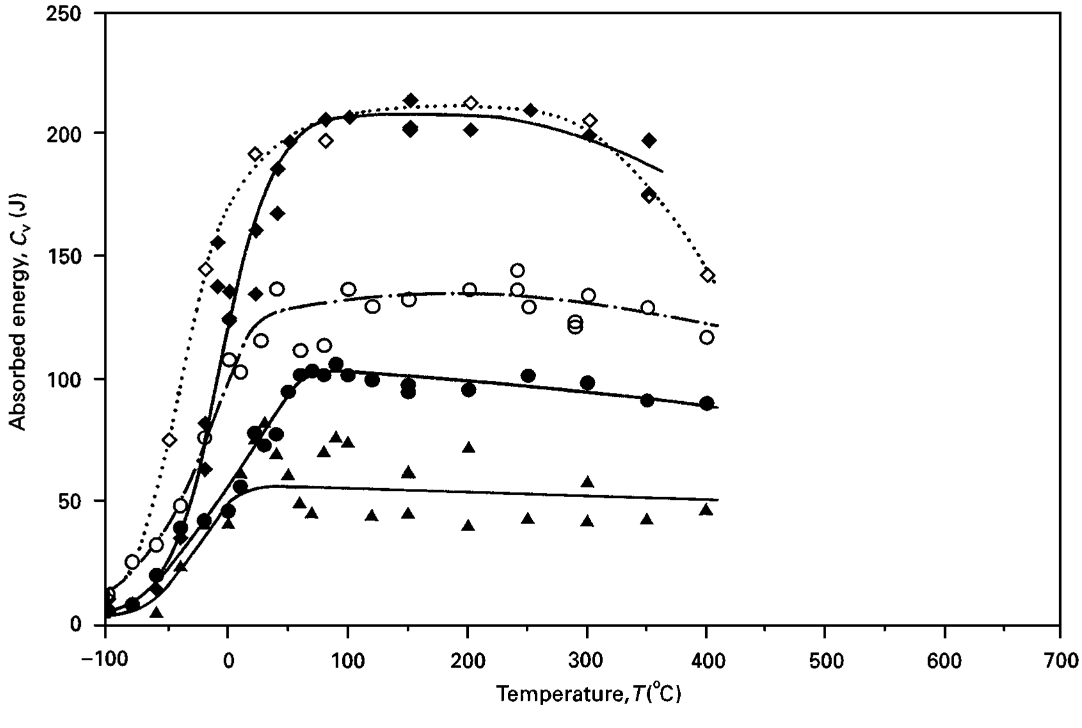

*Figure 5* $C_v$–T curves for the (◆, ●, ▲) 20 MnMoNi 5 5 base materials as well as for (○) the base material 22 NiMoCr 3 7 and (◇) the shape-welded material 10 MnMoNi 5 5. Transverse: (◆) 0.003% S, (●) 0.011% S, (▲) 0.020% S, (○) 0.006% S. S-position: (◇) 0.004% S, shape-welded 520 °C 20 h.

opening displacement, an effect which can be taken into account by introduction of a correction, $R_c$, for rotation. If $J$ is calculated according to ASTM E 813-81, and the rotation correction is taken into account for the determination of the crack extension, $\Delta a$, for each partial unloading, on the one hand, and, on the other hand, $J$ is calculated according to Ernst *et al.* [10] and rotation correction is not taken into account, the crack extension resistance curves, fitted in both cases to the measuring points by means of

TABLE VII Characteristic values of the tensile test as well as energy absorbed at room temperature and 150 °C

| Material | $T$ (°C) | $R_{p0.2}$ (N mm$^{-2}$) | $R_m$ (N mm$^{-2}$) | $A_5$ (%) | $Z$ (%) | $C_v$(J) Longitudinal | Transverse |
|---|---|---|---|---|---|---|---|
| X 20 CrMoV 12 1 | RT | 570 | 770 | 23 | 55 | 107 | 89 |
| (0.005% S) | 150 | 519 | 695 | 20 | 56 | 125 | 104 |
| X 20 CrMoV 12 1 | RT | 523 | 713 | 21 | 55 | 43 | 37 |
| (0.016% S) | 150 | 480 | 657 | 21 | 55 | 98 | 84 |
| X 20 CrMoV 12 1 | RT | 670 | 822 | 16 | 53 | – | 20[b] |
| similar weld metal | 150 | 615 | 748 | 14 | 53 | – | 62[b] |
| (550 °C/10$^4$ h)[a] | | | | | | | |
| 20 MnMoNi 5 5 | RT | 463[c] | 604 | 25 | 70 | 184 | 148 |
| (0.003% S) | 150 | 398[c] | 531 | 19 | 71 | 236 | 209 |
| 20 MnMoNi 5 5 | RT | 473[c] | 623 | 24 | 62 | 124 | 68 |
| (0.011% S) | 150 | 430[c] | 581 | 18 | 57 | 153 | 89 |
| 20 MnMoNi 5 5 | RT | 472[c] | 604 | 23 | 50 | 161 | 75 |
| (0.020% S) | 150 | 420[c] | 576 | 15 | 49 | 170 | 54 |
| 22 NiMoCr 3 7 | RT | 527 | 670 | 19 | 63 | 197 | 116 |
| (0.006% S) | 150 | 447 | 571 | 19 | 63 | 208 | 133 |
| 10 MnMoNi 5 5 | RT | 653[c] | 699 | 24 | 74 | 184 | 192[b] |
| shape-welded | 150 | 583[c] | 652 | 22 | 71 | 200 | 202[b] |
| (520 °C/20 h) | | | | | | | |

[a] Round tensile specimen DIN 50 125 - B 6 × 30.
[b] Charpy-V-specimen, S-position according to DIN 50 122.
[c] $R_{eH}$.

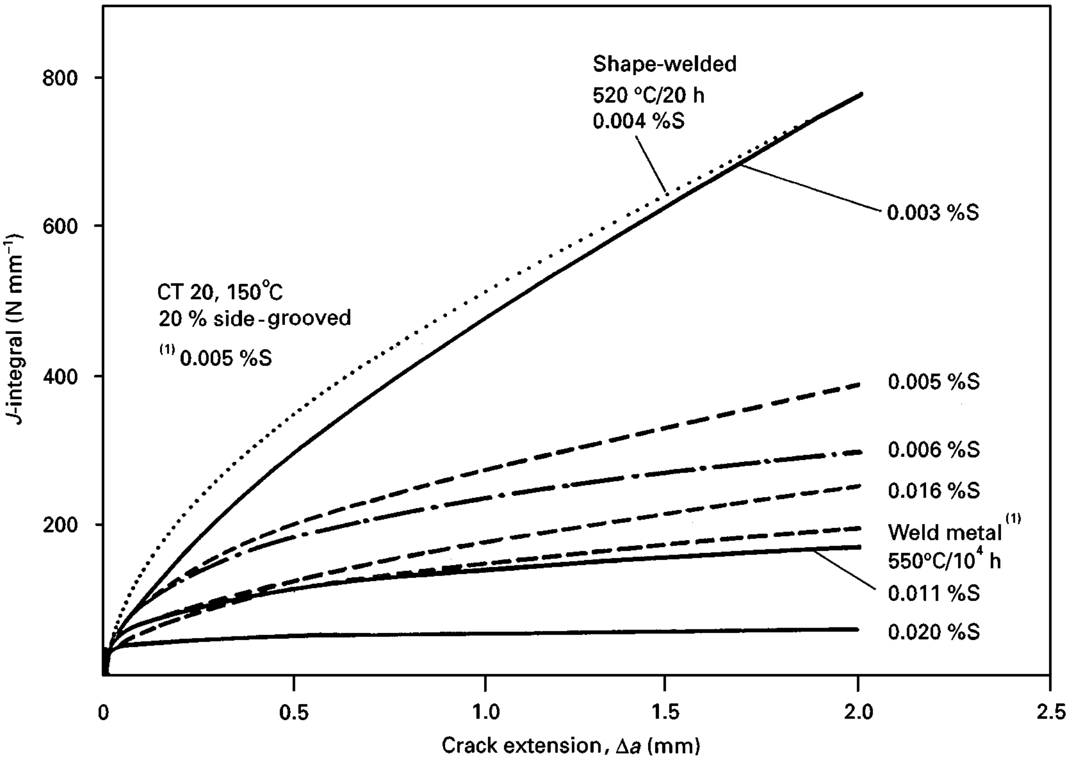

*Figure 6* J–R curves of all base materials and weld metals at 150 °C. (– – –) × 20 Cr MoV 12 1, (——) 20 MnMoNi 55, (– · –) 22 NiMoCr 3 7, (- - - -) 10 Mn MoNi 5 5.

a polynomial expression, can be seen as boundaries of a scatter band in which the J–R curves, obtained by a more recently developed evaluation method [11], are also included. Using this method, the J-integral was calculated according to Ernst, the crack extension Δa was determined considering the rotation correction, and the J–R curve was approximated by an exponential law of the type $J = C(\Delta a)^N$. The corresponding J–R curves of the X 20 CrMoV 12 1 materials are shown together with the J–R curves of the material 20 MnMoNi 5 5 and 22 NiMoCr 3 7 including the weld metal 10 MnMoNi 5 5, in Fig. 6. On comparing the $J$–$R$ curves of the X 20 CrMoV 12 1 materials, it is obvious that at large values of $\Delta a$, the optimized material has the highest $J$-values and the similar weld metal the lowest. The corresponding curves of the material 20 MnMoNi 5 5 show that the highest values of $J$ are achieved by the material with the lowest sulfur content (0.003% S), successively followed by the variants with 0.011% and 0.020% S. The material 22 NiMoCr 3 7 yields values significantly lower than those of the material 20 MnMoNi 5 5 with the lowest sulfur content; however, they are still higher than for the variant with 0.011% S. The highest values (slightly higher than those of the material with the lowest sulfur content) are shown by the shape-welded material 10 MnMoNi 5 5. The $J$-integrals, $J_{\mathrm{i,phys}}$, at physical crack initiation determined from the $J$–$R$ curves as the ordinates at the abscissa $\Delta a = \Delta a_{\mathrm{str}}$, where $\Delta a_{\mathrm{str}}$ is the stretched zone measured on the fracture surface of the compact tension specimen, are listed together with the $\Delta a_{\mathrm{str}}$-values for all materials in Table VIII. Both categories of steel show the same tendency: the stretched zone size as well as the $J$-integral, $J_{\mathrm{i,phys}}$, at physical crack initiation become smaller with increasing sulfur content.

## 3.4. Void initiation, growth and coalescence

The fracture process itself was investigated on round tensile specimens for all materials except the material 22 NiMoCr 3 7 using light optical and scanning electron microscopy. Tensile specimens of all materials were strained up to different values of elongation and some tensile specimens were loaded up to fracture. Then the specimens were cut in a plane containing the specimens' central axis which corresponds to the direction of the tensile load and therefore to the direction of maximum void growth. Subsequently, mechanically polished sections were prepared to allow observations of the actual state of void development. The size distributions of the voids were determined directly below the fracture surface on sections of which the plane was oriented transverse to the tensile direction.

The actual state of void development in tensile specimens strained up to fracture is represented in Fig. 7 for the steel 20 MnMoNi 5 5 (0.003% S) as well as for the shape-welded material 10 MnMoNi 5 5. Comparable to the results obtained for the X 20 CrMoV 12 1 materials [9], some large voids have been formed in the base material in contrast to many small voids in the shape-welded material. Voids in specimens strained up to different amounts are shown in Fig. 8 for the material 20 MnMoNi 5 5 with low sulfur content, and in Fig. 9 for the shape-welded material. In the specimens unloaded just beyond maximum load ($\varphi = 0.59$ for 20 MnMoNi 5 5, $\varphi = 0.22$ for 10 MnMoNi 5 5), voids have nucleated, in specimens unloaded at more extended deformation ($\varphi = 0.69$ for 20 MnMoNi 5 5, $\varphi = 1.09$ for 10 MnMoNi 5 5), only small void growth can be observed, while in

TABLE VIII Stretched zone and experimental $J_{\mathrm{i,phys}}$-values determined for 150 °C

| Material | CT 20 (20% Sg) stretched zone (μm) | $J_{\mathrm{i,\,phys}}$ experimental (N mm$^{-1}$) | | |
|---|---|---|---|---|
| | | ASTM with $R_c$ | Ernst mod. without $R_c$ | Erns mod. with $R_c$ |
| X 20 CrMoV 12 1 (0.005% S) | 39 | 79 | 105 | 81 |
| | 46 | 54 | 69 | 57 |
| | 43 | 43 | 74 | 59 |
| X 20 CrMoV 12 1 (0.016% S) | 18 | 24 | 29 | 26 |
| | 24 | 59 | 72 | 46 |
| | 19 | 24 | 29 | 23 |
| X 20 CrMoV 12 1 similar weld metal (550 °C/10$^4$ h) | 15 | 31 | 36 | 29 |
| | 15 | 16 | 20 | 21 |
| 20 MnMoNi 5 5 (0.003% S) | 88 | 77 | 120 | 85 |
| | 102 | 94 | 118 | 94 |
| 20 MnMoNi 5 5 (0.011% S) | 27 | 39 | 48 | 36 |
| | 33 | 46 | 58 | 46 |
| 20 MnMoNi 5 5 (0.020% S) | 19 | 19 | 26 | 20 |
| | 24 | 20 | 22 | 20 |
| 22 NiMoCr 3 7 (0.006% S) | 53 | 54 | 80 | 50 |
| | 43 | 49 | 74 | 51 |
| 10 MnMoNi 5 5 shape welded (520 °C/20 h) | 49 | 63 | 104 | 64 |
| | 50 | 69 | 120 | 69 |

$R_c$, correction for rotation, Sg, side grooved

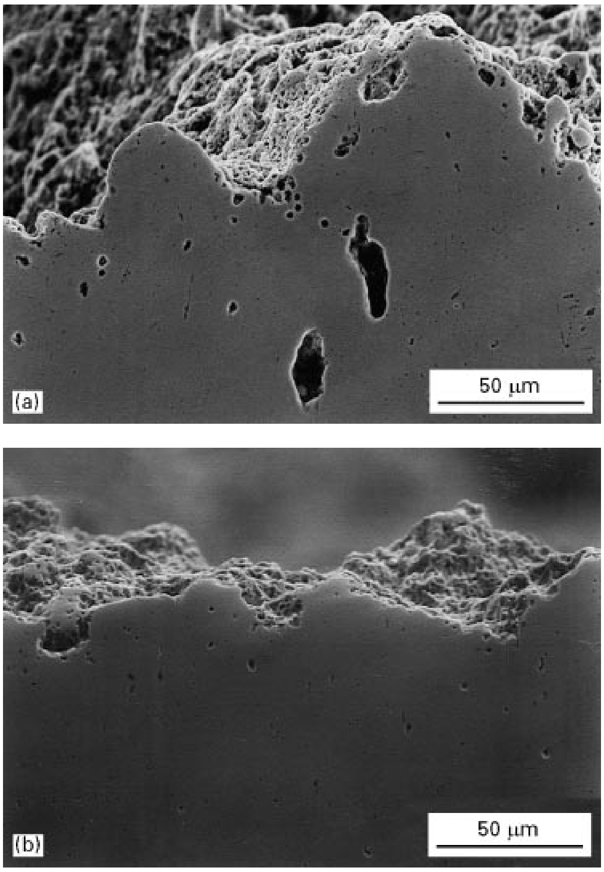

*Figure 7* Voids below the fracture surface of tensile specimens of (a) the base material 20 MnMoNi 5 5, (0.003% S); (b) the shape-welded material 10 MnMoNi 5 5.

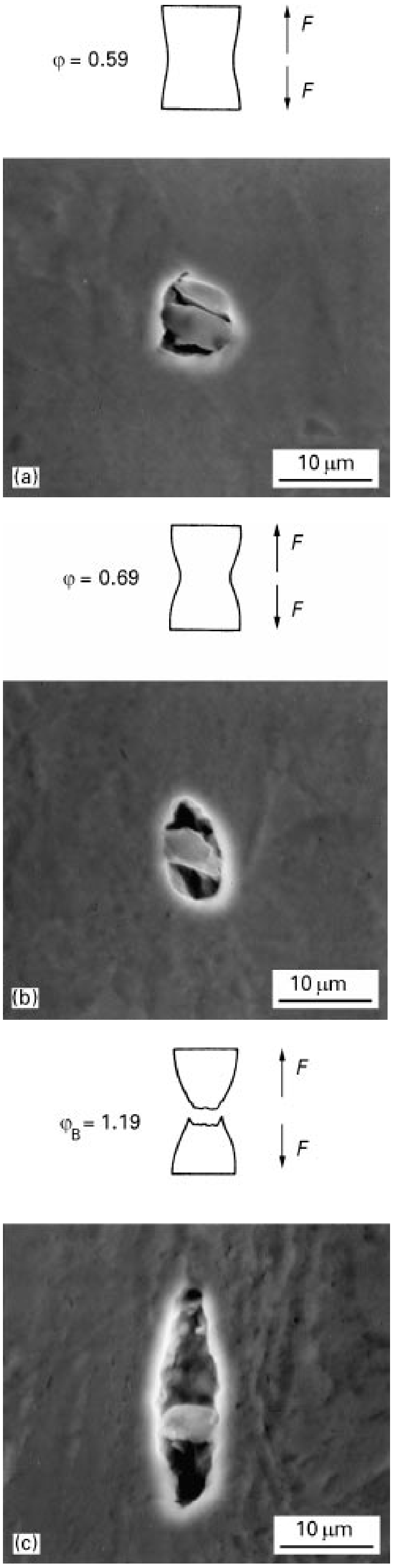

*Figure 8* Scanning electron micrographs of voids originating at non-metallic inclusions in tensile specimens ($T = 150\,^{\circ}\mathrm{C}$, $\dot{\varepsilon} = 4.4 \times 10^{-4}\,\mathrm{s}^{-1}$) loaded to different amounts of true strain $\varphi$ for the base material 20 MnMoNi 5 5 (0.003% S) ($\varphi_B$ is true strain at fracture, $F$ is force). Longitudinal section, mechanically polished.

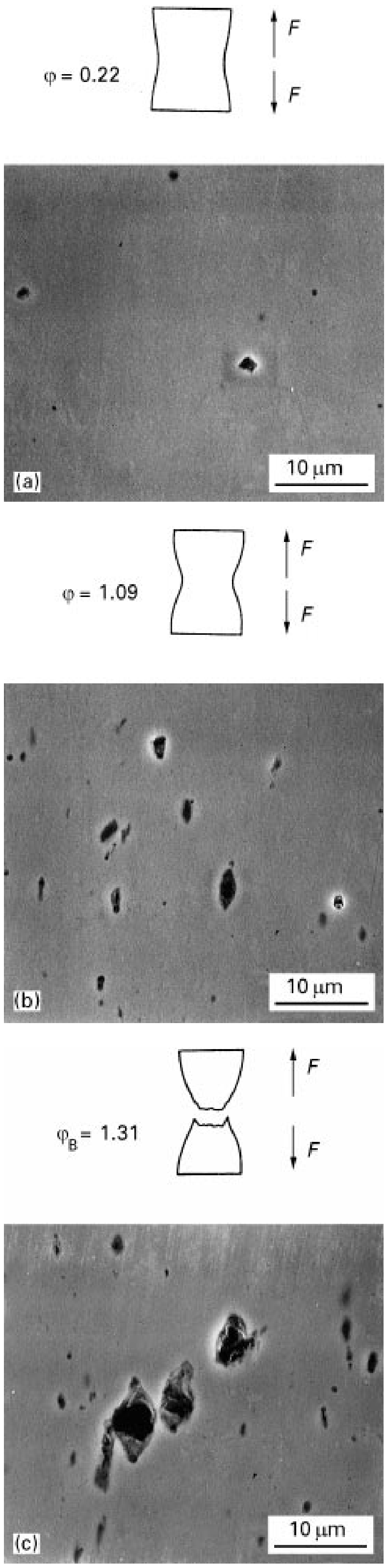

*Figure 9* Scanning electron micrographs of voids originating at non-metallic inclusions in tensile specimens ($T = 150\,^{\circ}\mathrm{C}$, $\dot{\varepsilon} = 4.4 \times 10^{-4}\,\mathrm{s}^{-1}$) loaded to different amounts of true strain, $\varphi$, for the shape-welded material 10 MnMoNi 5 5 ($\varphi_B$ is true strain at fracture, $F$ is force). Longitudinal section, mechanically polished.

the specimens loaded up to fracture ($\varphi_B = 1.19$ for 20 MnMoNi 5 5, $\varphi_B = 1.31$ for 10 MnMoNi 5 5), extensive void growth occurs. It can be recognized that in the base material as well as in the shape-welded material, voids develop in the same way.

## 3.5. Microstructure

The size distributions of the non-metallic inclusions were determined by means of a scanning electron microscope at a magnification of 4000 on mechanically polished longitudinal sections taken from the undeformed as-received materials and additionally on the fracture surfaces of the compact tension specimens. The plane of the sections was the L–S plane in the case of the base materials and the T–S plane in the case of the weld metals. For the determination of the large non-metallic inclusions, light optical microscopy was used. The size, $D_E$, of the non-metallic inclusions is the diameter in the case of spherical inclusions, and an equivalent diameter, as explained later, for elongated inclusions. This is also true for the size, $D_A$, of precipitates. Because the size of voids was determined on transverse sections through fractured tensile specimens, $D_H$ represents the diameter of the observed spheres. The size distributions of the voids are compared to the size distributions of the non-metallic inclusions taken from the fracture surface and from the polished section in Fig. 10 for the X 20 CrMoV 12 1 base materials and the similar weld metal, in Fig. 11 for the materials 20 MnMoNi 5 5, and in Fig. 12 for the shape-welded material 10 MnMoNi 5 5. For all

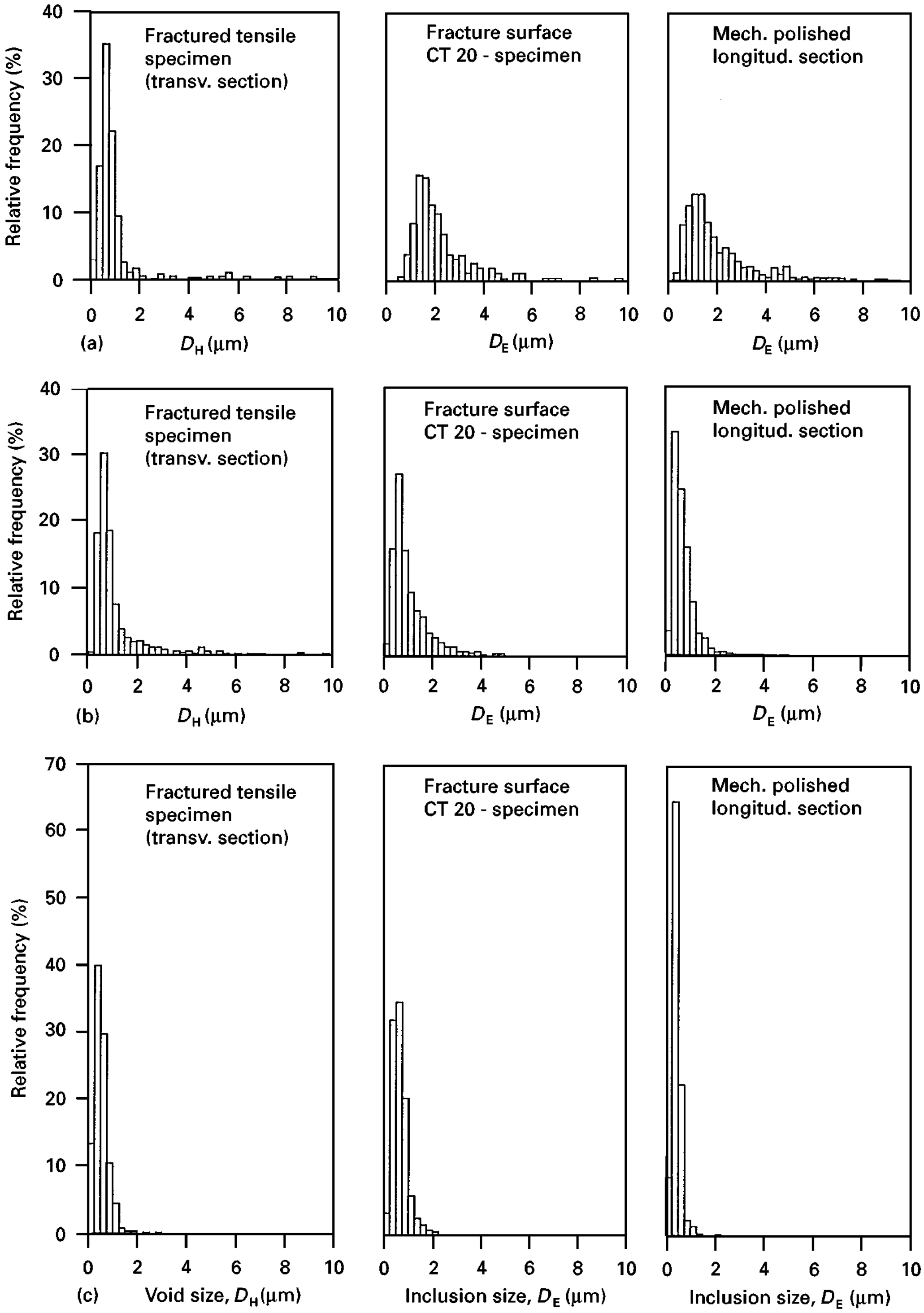

*Figure 10* Comparison of the size distribution of the voids with the size distributions of the non-metallic inclusions on the fracture surface as well as on a longitudinal section for (a, b) the X 20 CrMoV 12 1 base materials and (c) for the aged X 20 CrMoV 12 1-similar weld metal of the circumferential seam. (a) 0.005%, S, (b) 0.016% S, (c) 550 °C/$10^4$ h, 0.005% S.

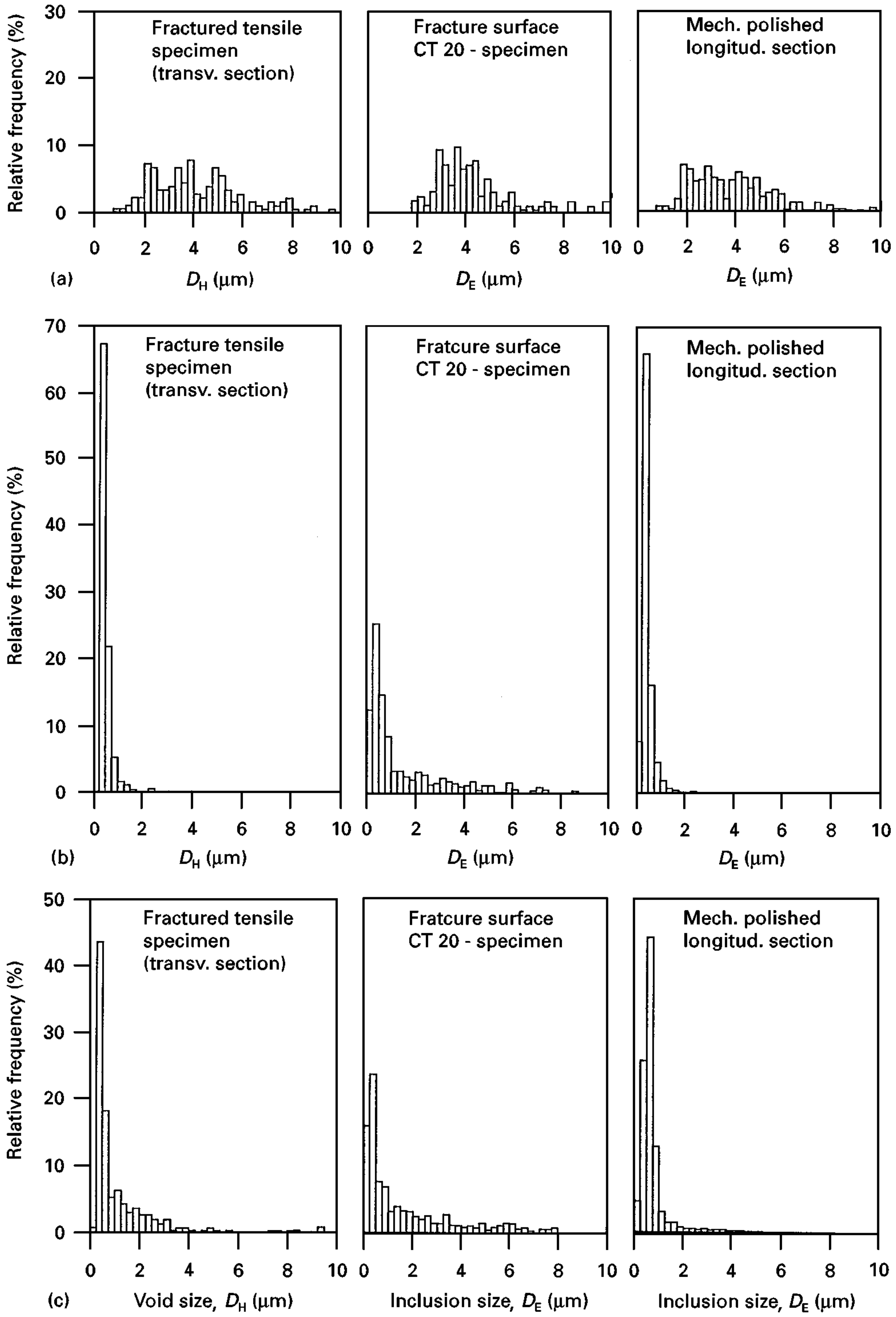

*Figure 11* Comparison of the size distribution of the voids with the size distributions of the non-metallic inclusions on the fracture surface, as well as on a longitudinal section for the 20 MnMoNi 5 5 base materials. (a) 0.003% S, (b) 0.011% S, (c) 0.020% S.

cases, the size distribution of the non-metallic inclusions determined on the fracture surface is practically the same as that determined on the polished section and corresponds to the size distribution of the voids. The histograms show a log-normal distribution. In comparison to the weld metals, the base materials evidently have larger inclusions and voids. The average number of the non-metallic inclusions per unit area was determined in the scanning electron microscope at a magnification of up to 4000 on polished transverse sections taken from the as-received materials. In the case of the base materials X 20 CrMoV 12 1 and 20 MnMoNi 5 5 (0.003% S) with larger inclusion sizes, light microscopy was also used. The total area used for counting was 10.5 mm$^2$ for the base material with the lowest inclusion density and 1 mm$^2$ for the weld metal with the highest inclusion density.

Precipitates of $M_{23}C_6$ were present in the material X 20 CrMoV 12 1, $Fe_3C$ and $Mo_2C$ in materials 20

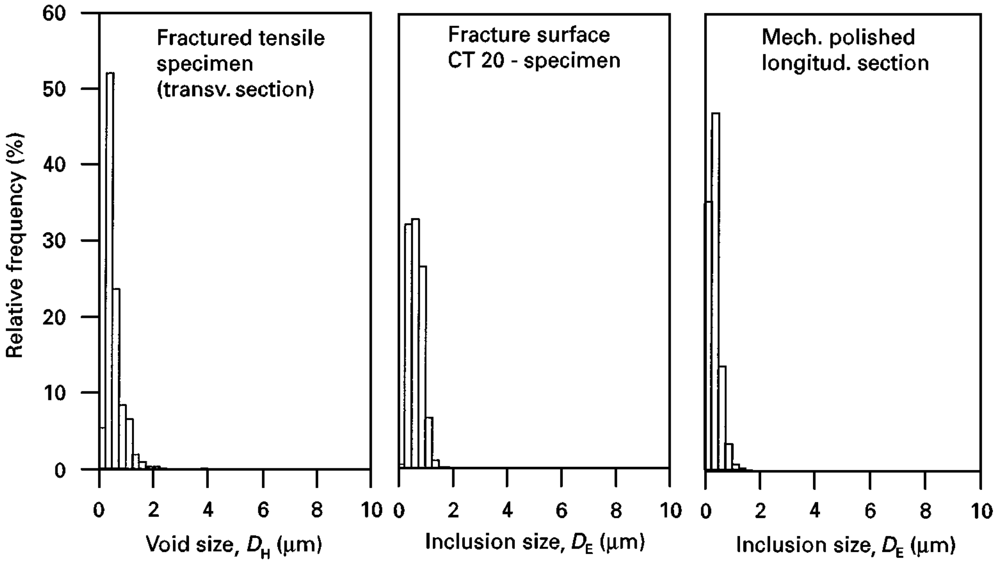

*Figure 12* Comparison of the size distribution of the voids with the size distributions of the non-metallic inclusions on the fracture surface, as well as on a longitudinal section for the shape-welded material 10 MnMoNi 5 5. 520 °C/20 h, 0.004% S.

MnMoNi 5 5 and 22 NiMoCr 3 7. In the shape-welded material 10 MnMoNi 5 5, $Fe_3C$ precipitates were also found, but $Mo_2C$-type precipitates were not identified. The size distributions of the precipitates were determined on extraction replicas, the number of precipitates per unit area was calculated using the number of precipitates per unit volume, which was determined on thinned metal foils. The size distributions for the $M_{23}C_6$ precipitates are represented in Fig. 13 and for the $Fe_3C$ precipitates in Fig. 14. The histograms show the size-distributions for the non-metallic inclusions as a log-normal distribution. Obviously for both groups of steels, the size distributions of the precipitates are situated at evidently smaller values compared to the size distributions of the non-metallic inclusions.

## 3.6. Calculation of $J_{\mathrm{i,phys}}$ using experimental data

The experimentally determined data necessary for the calculation of $J_{\mathrm{i,phys}}$ according to Equations 1 and 2, are compiled in Table IX. The average diameters of the non-metallic inclusions listed in this table were determined from the size distributions measured on the mechanically polished sections of the undeformed as-received materials by a special procedure. Bearing in mind that the size of a non-metallic inclusion measured on a section depends on the shape and on the relative position of the section plane with respect to the individual particle, further comments are necessary. Referring to the measured size, $D_E$, of the non-metallic inclusions in Figs 10–12, this size means the diameter for the circular inclusions which were dominant, especially in the weld metals. Elongated inclusions were approximated by an ellipse. The area of the ellipse was equalized to the area of a circle whose diameter is depicted. The same procedure was realized for the precipitates in Figs 13 and 14. The effect of the relative position of the section plane on the size of non-metallic inclusions was corrected by using the method of Saltykov [12]. Using the true diameter for the non-metallic inclusions or precipitates, the individual volume of each particle was calculated. By adding all these individual volumes, e.g. for the non-metallic inclusions for each size distribution, the total volume resulting for each size distribution was obtained. By dividing this total volume by the number of particles in each size distribution, an average volume for the average particle and, derived therefrom, the average diameter, $D_0$, listed in Table IX are obtained. In the case of the precipitates, the correction by the method of Saltykov was not necessary, because extraction replicas or metal foils were investigated. Using the data of Table IX, the $J$-integral at physical crack initiation was calculated for the materials investigated. The results of these calculations according to Equations 1 and 2 are represented, together with the experimentally determined $J_{\mathrm{i,phys}}$-values, in Table X.

## 4. Discussion and conclusions

The data compiled in Tables VII–X show that mainly with respect to toughness and microstructure, but also to the mechanical properties, a wide variety of materials and material conditions was investigated. With the exception of the shape-welded 10 MnMoNi 5 5 material, the fine-grained pressure vessel steels show lower values of yield and ultimate strength, as well as a less extensive work-hardening capacity, characterized by the ratio of these two quantities, compared to the heat-resistant X 20 CrMoV 12 1 materials. The elongation at fracture differs little between the two material categories, whereas higher values for the reduction of area and the true strain at fracture are achieved for the fine-grained pressure vessel steels, especially for those having the lower sulfur contents. For both weld metals, yield and ultimate strength are

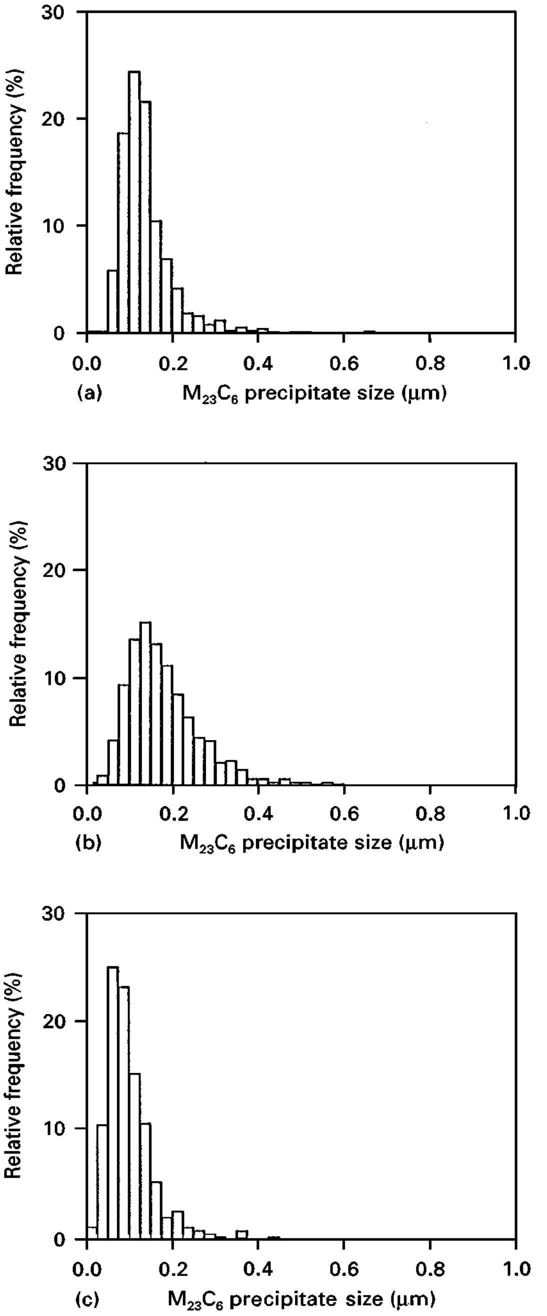

*Figure 13* Size distributions of the $M_{23}C_6$-precipitates of (a, b) the X 20 CrMoV 12 1 base materials and (c) the aged similar weld metal. (a) 0.005% S, (b) 0.016% S, (c) 550 °C/$10^4$ h, 0.005% S.

higher than for the corresponding base materials. Furthermore, the ratio of yield strength to ultimate strength is highest for the shape-welded material 10 MnMoNi 5 5.

Concerning the microstructural constituents, it should be noticed that the X 20 CrMoV 12 1 materials only contain precipitates of the $M_{23}C_6$ type, whereas the 20 MnMoNi 5 5 base materials and the base material 22 NiMoCr 3 7 show two types of precipitates, namely $Fe_3C$ and $Mo_2C$. Because of the short ageing time in the shape-welded material 10 MnMoNi 5 5, only $Fe_3C$-precipitates are found.

In contrast to the precipitates, the major part of the non-metallic inclusions in all materials show the same chemical composition and could be identified as MnS, $Al_2O_3$, $SiO_2$ and mixed ones. Only a few inclusions with other compositions occur, depending on the special accompanying elements of the particular heat. Size and density of the non-metallic inclusions vary, however, over a wide range. The non-metallic inclusions of the weld metals are much smaller than those of the base materials. In the base materials, both types of steel show a similar behaviour. Materials with lower sulfur content show lower densities of non-metallic inclusions but, at the same time, the inclusions are larger. Comparing the size and the size distribution as well as the density of the non-metallic inclusions to those of the precipitates, it becomes obvious for all materials that the precipitates are considerably smaller, whereas the density is higher by several orders. Furthermore, the $Mo_2C$ precipitates are smaller than the $Fe_3C$ precipitates.

The wide range of toughness of the investigated materials is documented by the absorbed energy in the upper shelf as well as by the $J$-integral, $J_{\mathrm{i,phys}}$, at physical crack initiation. In the base materials, a distinct dependence can be seen between sulfur content and the fracture mechanics parameters. For both types of steel, the absorbed energy as well as the stretched zone width and the $J$-integral, $J_{\mathrm{i,phys}}$, decrease with increasing sulfur content. Moreover, it should be mentioned that the material 22 NiMoCr 3 7 fits well into the group of the 20 MnMoNi 5 5 materials.

Although important differences exist between the investigated materials, the micrographs representing the actual state of void development in tensile specimens strained up to different amounts of true strain as well as up to fracture, show that the fracture process for all materials under consideration is really the same. Therefore, the calculation of $J_{\mathrm{i,phys}}$ was allowable according to the two relations described above which are based on this type of fracture process. Comparing the $J_{\mathrm{i,phys}}$ values calculated according to the modified Stroppe equation with the $J_{\mathrm{i,phys}}$-values experimentally determined at 150 °C, it is shown that the calculated values fall into the scatterband of the experimentally determined ones, which means a good agreement of calculated and measured values. The calculated values according to the modified Hahn and Rosenfield relation for only one material, the X 20 CrMoV 12 1 with low sulfur content, correspond to the measured one. In all other cases no correspondence is found.

The main conclusion which results is that for the first time it was possible to relate quantitatively, using an analytical equation, microstructural parameters with physical crack initiation characterized by $J_{\mathrm{i,phys}}$, for materials and material conditions from low to high toughness. This holds not only for base materials with different sulfur contents, but also for weld metals of different kinds. The importance of the size and density of the non-metallic inclusions is underlined quantitatively for the investigated steel types, with the consequence that size times density is the decisive parameter for toughness.

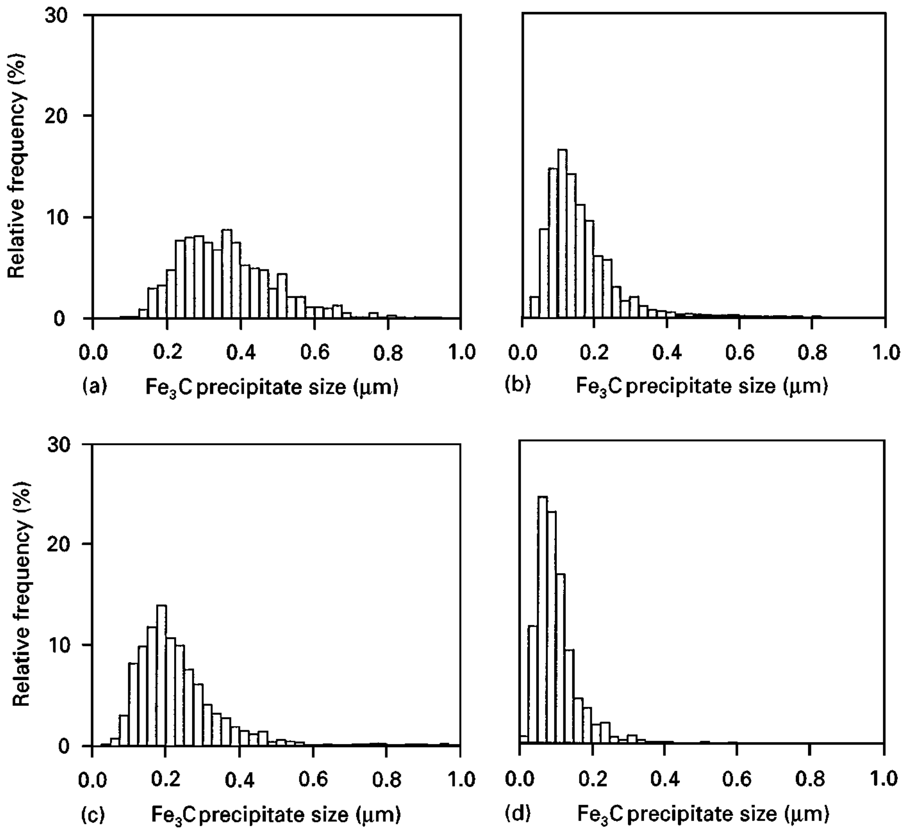

*Figure 14* Size distributions of the $Fe_3C$-precipitates of (a–c) the 20 MnMoNi 5 5 base materials and (d) the shape-welded material 10 MnMoNi 5 5. (a) 0.003% S, (b) 0.011% S, (c) 0.020% S, (d) 520 °C/20 h, 0.004% S.

TABLE IX Data of the tensile test and microstructural data required for the calculation of the $J$-integral at physical crack initiation

| Material | Tensile test T = 150 °C | | | | Carbides TEM | | | Inclusions section | |
|---|---|---|---|---|---|---|---|---|---|
| | $R_{p0.2}$ (N mm$^{-2}$) | $k_H$ (N mm$^{-2}$) | $n_H$ | $\varphi_B$ | Type | $N_E$ ($10^6$ mm$^{-2}$) | $D_0$ (µm) | $N_E$ (mm$^{-2}$) | $D_0$ (µm) |
| X 20 CrMoV 12 1 (0.005% S) | 500 | 1002 | 0.126 | 0.77 | $M_{23}C_6$ | 8 | 0.142 | 369[a] | 3.4 |
| X 20 CrMoV 12 1 (0.016% S) | 481 | 1002 | 0.150 | 0.79 | $M_{23}C_6$ | 6.6 | 0.140 | 816 | 2.0 |
| X 20 CrMoV 12 1 similar weld metal (550 °C/$10^4$ h) | 615 | 1005 | 0.096 | 0.76 | $M_{23}C_6$ | 6.1 | 0.087 | 10048 | 0.6 |
| 20 MnMoNi 5 5 (0.003% S) | 417 | 800 | 0.125 | 1.19 | $Fe_3C$<br>$Mo_2C$ | 4.5<br>53 | 0.266<br>0.040 | 188 | 4.9 |
| 20 MnMoNi 5 5 (0.011% S) | 430 | 832 | 0.124 | 0.86 | $Fe_3C$<br>$Mo_2C$ | 2.6<br>5.5 | 0.171<br>0.035 | 3051 | 0.9 |
| 20 MnMoNi 5 5 (0.020% S) | 441 | 838 | 0.123 | 0.62 | $Fe_3C$<br>$Mo_2C$ | 2.2<br>6.7 | 0.174<br>0.034 | 3353 | 1.3 |
| 22 NiMoCr 3 7 (0.006% S) | 447[b] | 932 | 0.197 | 1.00 | $Fe_3C$<br>$Mo_2C$ | 1.7<br>4.7 | 0.174<br>0.027 | 1294 | 1.2 |
| 10 MnMoNi 5 5 shape-welded (520 °C/20 h) | 583[b] | 1075 | 0.158 | 1.31 | $Fe_3C$ | 2.1 | 0.175 | 3340 | 0.5 |

[a] Average of the values measured for two occurring patterns: 169 and 570 mm$^{-2}$, respectively.

[b] $R_{eH}$.

TABLE X Comparison of experimental $J_{i,phys}$-values determined for 150 °C with calculated $J_{i,phys}$-values

| Material | $J_{i,\,phys}$ experimental[a] ($N\,mm^{-1}$) | | | $J_{i,\,phys}$ calculated ($N\,mm^{-1}$) | |
|---|---|---|---|---|---|
| | ASTM with $R_c$ | Ernst mod. without $R_c$ | Ernst mod. with $R_c$ | Stroppe mod.[b, c] | Hahn and Rosenfield mod.[d] |
| X 20 CrMoV 2 1 (0.005%S) | 79<br>54<br>43 | 105<br>69<br>74 | 81<br>57<br>59 | 78 | 93 |
| X 20 CrMoV 12 1 (0.016% S) | 24<br>59<br>24 | 29<br>72<br>29 | 26<br>46<br>23 | 59 | 131 |
| X 20 CrMoV 12 1 similar weld metal (550 °C/$10^4$ h) | 31<br>16 | 36<br>20 | 29<br>21 | 17 | 60 |
| 20 MnMoNi 5 5 (0.003% S) | 77<br>94 | 120<br>118 | 85<br>94 | 89 | 118 |
| 20 MnMoNi 5 5 (0.011% S) | 39<br>46 | 48<br>58 | 36<br>46 | 37 | 99 |
| 20 MnMoNi 5 5 (0.020% S) | 19<br>20 | 26<br>22 | 20<br>20 | 28 | 68 |
| 22 NiMoCr 3 7 (0.006% S) | 54<br>49 | 80<br>74 | 50<br>51 | 59 | 267 |
| 10 MnMoNi 5 5 shape welded (520 °C/20 h) | 63<br>69 | 104<br>120 | 64<br>69 | 65 | 299 |

[a] $T = 150\,°C$.

[b] Contribution of carbides $< 1\,N\,mm^{-1}$.

[c] $$J_{i,\,phys} = \frac{k\varphi_B^{n+1}}{\pi(n+1)e^{\varphi_B}}\frac{1}{N_E D_0}$$

[d] $$J_{i,\,phys} = \frac{2}{3}25.4\,mm\,(1 - \nu^2)R_e\varphi_B n^2$$

## Acknowledgements

The investigations were realized within the scope of a research project of the Ministry for Research and Technology (BMFT), and with support of the Alfried Krupp von Bohlen und Halbach foundation.

## References

1. R. H. VAN STONE, T. B. COX, J. R. LOW Jr. and J. A. PSIODA, *Int. Met. Rev.* **30** (1985) 157, and literature cited therein.
2. P. F. THOMASON, "Ductile fracture of metals" (Pergamon Press, Oxford, New York, Beijing, Frankfurt, Sao Paulo, Sydney, Tokyo, Toronto, 1990).
3. P. DEIMEL, W. BURR, H. FISCHER, D. KUPPLER and E. SATTLER, Final report, MPA-contribution, BMFT-project Nr. 1500 748, 2. Partial project, December 1991, and literature cited therein.
4. H. STROPPE, *Neue Hütte* **26** (1981) 446.
5. G. T. HAHN, and A. R. ROSENFIELD, ASTM STP 432, (American Society for Testing and Materials, Baltimore, MD, 1968) p. 5.
6. A. S. ARGON, "Topics in fracture and fatigue" (Springer Verlag, New York, Berlin, Heidelberg, 1992).
7. J. C. LAUTRIDOU and A. PINEAU, *Engng. Fract. Mech.* **95** (1981) 55.
8. P. DEIMEL, W. BURR, D. KUPPLER and E. SATTLER, Final report, MPA-contribution, BMFT-project Nr. 1500 6563, 1. Partial project, December 1985.
9. P. DEIMEL and E. SATTLER, *Nucl. Engng. Design* **144** (1993), 9.
10. H. A. ERNST, P. C. PARIS and J. D. LANDES, ASTM STP 743, edited by R. Roberts (American Society for Testing Materials, Philadelphia, PA, 1981) p. 476.
11. E. ROOS, M. SEIDENFUSS, D. KRÄMER, S. KROLOP, U. EISELE und U. HINDENLANG, *Nucl. Engng. Design* **130** (1991) 297.
12. S. A. SALTYKOV, "Stereometrische Metallografie" (VEB Deutscher Verlag für Grundstoffindustrie, Leipzig, 1974).

*Received 9 June*
*and accepted 5 December 1997*